Citation: Yuan, Y., Ma, Q., Yan, S., Zheng, X., Liao, K., Ma, G., Sun, H. & Khayyer, A. (2023). A hybrid method for modelling wake flow of a wind turbine. Ocean Engineering, 281, 114770. doi: 10.1016/j.oceaneng.2023.114770

This is the published version of the paper.

This version of the publication may differ from the final published version. To cite this item please consult the publisher's version.

Permanent repository link: https://openaccess.city.ac.uk/id/eprint/30502/

Link to published version: https://doi.org/10.1016/j.oceaneng.2023.114770

Ocean Engineering 281 (2023) 114770

Contents lists available at ScienceDirect

Ocean Engineering

journal homepage: www.elsevier.com/locate/oceaneng

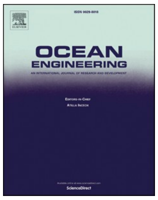

A hybrid method for modelling wake flow of a wind turbine

Yuming Yuan[a], Q.W. Ma[b,*], Shiqiang Yan[b], Xing Zheng[a], Kangping Liao[a], Gang Ma[a], Hanbing Sun[a], Abbas Khayyer[c]

[a] Harbin Engineering University, China
[b] School of Science and Technology, City, University of London, London, UK
[c] Kyoto University, Japan

ARTICLE INFO

Handling Editor: Prof. A.I. Incecik

Keywords:
Offshore wind turbine
Turbine wake modelling
Dynamic wake models
Turbine aerodynamics

ABSTRACT

A fast and accurate prediction of the wake of an upwind turbine is very important to quantify the performance of downwind turbines in offshore wind farms, which become larger and larger. The wake flow and dynamics may be quite accurately simulated by high-fidelity computational fluid dynamics (CFD) software but its computational costs are too high, in particular to simulate a long wake flow often required in engineering practice. Therefore, the wake is often modelled by simplified dynamic wake models in design practices. They are computationally efficient but could not catch all physics, depend on pre-specified empirical parameters, and are not suitable for flow near the turbine. This paper proposes a new hybrid method, in which the near wake flow is simulated by a CFD model based on Navier–Stokes equations with the turbine represented by actuator lines while the far wake flow is modelled by an improved simplified CFD-based dynamic wake model. The two models are two-way coupled at a section downwind the turbine. The newly formulated method is validated by the results of full CFD simulations in the whole domain. Its performances are investigated under different conditions. It will be demonstrated that the new method takes considerably less computational time than the full CFD tool to produce similar results.

1. Introduction

Wind energy has contributed significantly to daily energy consumption and will contribute more in future. To maximise the economic efficiency of energy production, the wind turbines are generally grouped in farms. Wind farms become larger and larger, in particular in offshore areas. The optimal wind turbine spacing in wind farms has attracted a great interest and been found to be ~15*D*, where *D* is the diameter of wind turbine, based on the ratio of land surface costs and turbine costs (Meyers and Meneveau, 2012). Considering other factors, such as transmission lines, typically operational turbine spacing is generally selected to be 6-10*D* (Howland et al., 2019). At such spacing, the wake of upwind turbines can significantly affect the dynamics of downwind turbines. In particular, the reduced wind speed in the wake of upwind turbines can decrease the energy production of downwind turbines, and the added turbulence produced by upwind turbines can shorten the lifetime of downwind turbines. Therefore, the wake models are needed to faithfully reproduce the wake of upwind turbines for correct evaluation of the downwind turbine performance that are essential for designing, operating and maintaining wind farms.

Great efforts have been made in developing the wake models for studying the wake flow of turbines. These models may be classified into three categories: analytical modelling, simplified CFD-based modelling and full CFD-based modelling. Each of them is briefly discussed below.

Analytical modelling provides analytical equations for estimating the wind velocity in the wake of turbines. The relevant work has been extensively reviewed and discussed in literature, for example, by Archer et al. (2018) and Neiva et al. (2019). Some analytical models are briefed here. The analytical model in Jensen (1983) gave an equation for estimating the wake deficit, i.e., the axial wind speed reduction (or wake loss) in the wake of a turbine, with an empirical parameter. The equation assumes that the wake is an axisymmetric and expands linearly along the axial direction, and that the axial velocity is only a function of axial positions, independent of radial positions. Frandsen et al. (2006) proposed an analytical model allowing nonlinear expansion of wake. Larsen (1988) developed a more advanced analytical wake model which does not only consider axial positions but also radial positions. Later, a Gaussian-like model was suggested by Bastankah and Porté-Agel (2014).

---

* Corresponding author.
E-mail address: q.ma@city.ac.uk (Q.W. Ma).

https://doi.org/10.1016/j.oceaneng.2023.114770
Received 16 February 2023; Received in revised form 12 April 2023; Accepted 4 May 2023

In this wake model, the wake loss has a Gaussian shape with the same expansion rate in the vertical and horizontal directions with one empirical parameter involved. Similarly, Xie and Archer (2015) proposed a Gaussian-type wake loss model allowing different expansions in the horizontal and vertical directions. All these models concern only about the axial velocity, ignore the radial and tangential velocities and assume that the flow in the wake is stationary.

Simplified CFD-based modelling provides a set of equations to be solved numerically. One of them in this category is the linearised model prosed by Ott (2011). The equations in this model are derived from the Navier-Stokes equations by dropping the term of time derivatives, i.e., assuming the problems to be stationary, and using a forcing term to represent the effects of turbines (called an actuator disk model). The equation is linearised against the disturbance of the forcing term. A widely used model in this category is that proposed by Ainslie (1988), including a set of equations for solving axial and radial velocity in wake. The equations are derived by assuming that the flow in wake is axisymmetric and stationary without considering the tangential velocity and pressure gradient. This model was extended by Jonkman and Shaler (2021), being able to model wake advection (evolution), deflection and meandering in a quasi-steady manner.

Full CFD-based modelling is to solve the full set of Navier-Stokes equations in the time and space domain with the turbulence to be modelled by RANS-based turbulence models or by Large Eddy Simulation (LES) models. Good reviews on the models may be found in literature, such as Sanderse et al. (2011), Mehta et al. (2014) and Porté-Agel et al. (2020). In the models, the wind turbine is represented by an actuator disk, an actuator line or surface (e.g, Calaf et al., 2010 and Sørensen et al. ,2002), or the geometry of the turbine is fully resolved (e.g., Wuβow et al., 2007). The performance of different models was assessed by Adaramola and Krogstad (2011) for one turbine and by Pierella et al. (2014) for two turbines.

Generally speaking, the analytical models are very computationally efficient even for dealing with a long wake (such as more than 10*D*), but they ignore some important physics and depend on empirical factors. It would be questionable if they are applied in the near wake region, such as less than 2*D* from turbines. Simplified CFD-based models consider more physics, such as considering radial velocity and wake evolution behaviours (Jonkman and Shaler, 2021) and require more computational resources than the analytical models. Nevertheless, their computational efficiency is still acceptable. They also depend on empirical parameters, may not be suitable for the near wake flow and could not produce spiral phenomenon in the wake due to ignoring the tangential velocity. Full CFD-based models can catch all the physics more accurately at least in theory. However, they take prohibitive computational time (e.g., $\sim 10^3$–10^4 h per simulation as indicated by Porté-Agel et al., 2020) even with very advanced computers, in particular for modelling a long wake, such as more than 6*D*.

This paper proposes a new hybrid method which can be more accurate than simplified CFD-based model but requires considerably less computational time than the full CFD-based models. The main idea is that in the near wake of the turbine, a full CFD-based model is applied with the turbine represented by actuator lines while the simplified CFD-based model is employed in the far wake. To better catch the physics, the employed wake model will be improved. The hybrid method will be validated by using the results of full CFD-based model in whole computational domain, and its performances will be studied for different operational conditions. It will be demonstrated that the hybrid method can save considerable computational time than a full CFD-based model while achieving similar results. As it is the first paper introducing the hybrid method, we only consider a single fixed turbine without ocean waves. More complex cases will be studied in our future work with necessary extension.

2. Numerical models

The new hybrid method to be developed will be formed by coupling two kinds of numerical model: the full Navier–Stokes (NS) model in the near wake of the turbine combined with a dynamic wake model (DWM) in the far wake as indicated above. It is illustrated in Fig. 1. The flow in the area (Ω_{NS}) covered by the solid line is solved by the full NS model while the flow in the area (Ω_{DWM}) covered by the dashed line is solved by an DWM. The two areas overlap with each other. The overlapping area is called coupling zone. For convenience, the downstream boundary (its axial coordinate denoted by x_{c2}) of the coupling zone is called coupling boundary and the upwind boundary (its axial coordinate denoted by x_{c1}) of the coupling zone is called 'DWM inlet'. The length of the coupling zone, x_{c2} -x_{c1}, needs to be assigned properly. If it would be too long, the NS domain will be unnecessarily too big and so the NS model will take unnecessarily long computational time. If it would be too short, the transition of variables in the zone would be too rapid, leading possibly to large errors. The length of the coupling zone is taken as 0.5D in this paper based on our numerical tests. There is a dash-dotted line in the figure which will be explained later. The figure also shows the coordinate systems to be used: Cartesian coordinate system (*x,y,z*) and cylindrical coordinate system (*x, r, θ*). The origins of the systems are at the centre of the turbine hub with x-axis pointing to the flow direction of wind, z-axis points upward and θ is positive in the anti-clock direction when viewed facing the incoming wind. In the systems, the flow velocity vector ($\vec{u}$) is expressed by $\vec{u} = (V_x, V_y, V_x)$ or $\vec{u} = (V_x, V_r, V_\theta)$, with V_x, V_y, V_x being the velocity components in the *x*-*y*-z system, and V_x, V_r, V_θ being the velocity components in the *x*-*r*-*θ* system. They are easily transformed from one to another.

2.1. NS model and CFD (ALM)

The simulation of flow in the Ω_{NS} is based on the incompressible solver in OpenFOAM using the combined PISO-SIMPLE (PIMPLE)algorithm. This formulation is well-known. The details can be found in the documentation of OpenFOAM. For completeness, only brief introduction is given below. The governing equations to be used are the Reynolds averaged Navier Stokes equation (RANS) :

$$\nabla \cdot \vec{u} = 0 \tag{1a}$$

$$\frac{\partial \rho \vec{u}}{\partial t} + \nabla \cdot \left[\rho\left(\vec{u} - \vec{U}_g\right)\vec{u}\right] = -\nabla p - \rho \boldsymbol{g} + \nabla \cdot (\mu \nabla \vec{u}) + \rho \boldsymbol{f}_{UALM} \tag{1b}$$

where ρ is the fluid density; $\vec{U}_g$ is the computational grid velocity; p is the dynamic pressure; g is the vector of the gravitational acceleration; $\boldsymbol{f}_{UALM}$ is the source term to model the blade effects on the fluids; $\mu = \mu_d + u_t$ with μ_d being dynamic viscosity and u_t the turbulent viscosity. The turbulent viscosity is estimated by solving the standard k-ω SST (shear stress transfer) turbulence model in the OpenFOAM (Menter et al., 2003), which will not be detailed further.

The interaction between flow and turbine is modelled by using an actuator line model (ALM) proposed by Sørensen and Shen (2002). In the model, the aerodynamic forces on the turbine blades are estimated by using a well-known blade element method. The effect of the turbine blades on the flow dynamics is modelled by distributing the aerodynamics forces as a body force ($\rho \boldsymbol{f}_{UALM}$) into the flow domain. More details can be found in the above reference.

The NS model combined with ALM is named as CFD (ALM) hereafter. For the purpose of comparison, the CFD (ALM) may be used alone, i.e., the flow in the whole domain is solved by this model without use of DWM.

2.2. Existing dynamic wake model (DWM) and CFD (ALM)-DWM

Many dynamic wake models can be found in literature as indicated

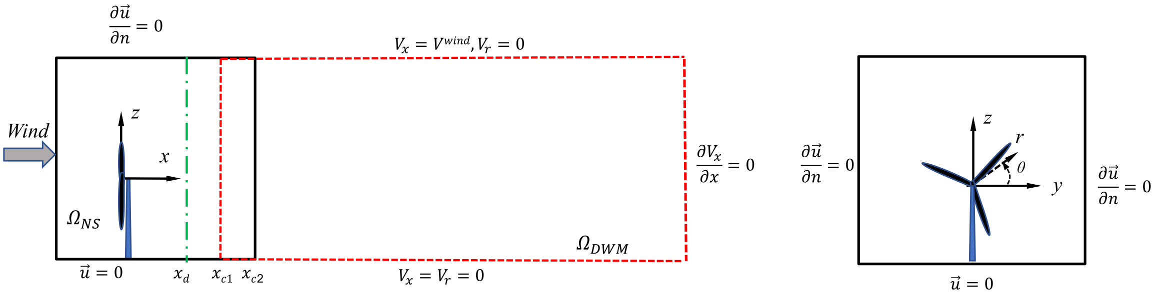

(a) Side view

(b) View from x-axis direction

Fig. 1. Illustration of the new hybrid method (NS model used in the solid-line area while DWM used in the dashed-line area; the lower boundary represents the water surface; the upper boundary is the artificial cut-off boundary).

above. The model proposed by Ainslie (1988) and extended by Jonkman and Shaler (2021) will be employed here. For convenience of discussion, the extended model is called as existing dynamic model hereafter and is briefed next. This model gives a set of equations in the cylindrical coordinate system obtained by simplifying the Navier–Stokes equations without the pressure terms and assuming that the wake flow is axisymmetric, stationary and $V_\theta = 0$. The equations used in this model are

$$V_x\frac{\partial V_x}{\partial x} + V_r\frac{\partial V_x}{\partial r} = \left(\frac{1}{r}\right)\frac{\partial}{\partial r}\left(r v_t \frac{\partial V_x}{\partial r}\right) \tag{2}$$

$$\frac{\partial V_x}{\partial x} + \frac{1}{r}\frac{\partial}{\partial r}(rV_r) = 0 \tag{3}$$

where v_t is the empirical kinematic eddy viscosity varying spatially to approximate the turbulent effects in the wake flow and estimated by

$$v_t(x,r) = F_{v_{Amb}}(x) k_{v_{Amb}} I_{Amb} V^{wind} R + F_{v_{Shr}}(x) k_{v_{Shr}} R^{wake} MIN|_r\{V_x(x,r)\}, \tag{4a}$$

in which $F_{v_{Amb}}(x)$ is the filter function associated with ambient turbulence and $F_{v_{Shr}}(x)$ the filter function associated with the wake shear as discussed in the cited reference. They are applied in a region near the turbine. In this paper the model is applied downwind the DWM-inlet that is at a distance away from the turbine. Therefore, it is reasonable to assume that both functions can be taken as one. As a result, the above equation can be changed to

$$v_t(x,r) = k_{v_{Amb}} I_{Amb} V^{wind} R + k_{v_{Shr}} R^{wake} MIN|_r\{V_x(x,r)\}, \tag{4b}$$

where I_{Amb} is the turbulence intensity at hub centre evaluated in the same way as that proposed by Jonkman and Shaler (2021); $MIN|_r\{V_x(x,r)\}$ denotes the minimum value of V_x along the radius at a given downstream section; $k_{v_{Amb}}$ and $k_{v_{Shr}}$ are coefficients associated with the influence of ambient turbulence and wake shear layer on the eddy viscosity, specified as 0.05 and 0.016, respectively, following the suggestion of the cited reference. In the above equations, R^{Wake} is the wake half-width estimated by

$$R^{wake}(x) = MAX\left\{D\big/2, r|_{\{V_x(x,r)=0.99V^{wind}\}}\right\} \tag{4c}$$

where V^{wind} is the incoming wind speed. For convenience of discussion below, the axial velocity (V_x) in the wake may be expressed by

$$V_x = V^{wind} + V_x^{Wake} \tag{5}$$

According to Jonkman and Shaler (2021), Eqs. (2) and (3) are solved using the averaged and filtered physical quantities at the turbine section as their inlet conditions, and allowing the wake to gradually evolve to the downwind. Due to this feature, the time-dependent behaviour of wake is partially modelled. Other features of the model can be found in the cited reference.

The existing dynamic model may be combined with CFD (ALM) and used to solve the flow in Ω_{DWM}. They are coupled in the same way as discussed in the following section. The resulted model will be called as CFD (ALM)-DWM hereafter. The main differences between the dynamics wake model used in CFD (ALM)-DWM from the one in Jonkman and Shaler (2021) are that (1) the inlet of DWM is a section at a distance downwind the turbine rather than at the turbine and (2) the information between CFD (ALM) and DWM is exchanged through the coupling zone in the way discussed in the following section, i.e., the solution from the DWM affecting the solution of CFD (ALM). It is obvious that the tangential velocity in the wake flow after coupling boundary is zero in this model.

2.3. *Improved dynamic wake model (IDWM) and CFD (ALM)-IDWM*

The new hybrid method proposed in this paper is formed by coupling CFD (ALM) with a new improved dynamic wake model (IDWM), based on but different from the one described in Section 2.2. As has been seen in the above discussions, the existing DWM ignores the tangential velocity entirely, and specifies a fixed value to $k_{v_{Shr}}$ prior to the modelling. Our numerical tests, some of which will be presented in Section 4, have shown that these imperfect aspects can affect the results of wake flow considerably. We firstly describe how these two aspects are improved below.

The equations for solving the axial and radial velocity for IDWM are the same as Eqs. (2), (3) and (4b). However, the coefficient $k_{v_{Shr}}$ is evaluated using the results from CFD (ALM). For this purpose, Eq. (2) is integrated with respect to the radial coordinate at the DWM inlet (i.e., $x = x_{c1}$), also considering Eq. (4b), to give

$$\int_0^{R^{wake}}\left(V_x\frac{\partial V_x}{\partial x} + V_r\frac{\partial V_x}{\partial r}\right) rdr = k_{v_{Amb}} I_{Amb} V^{wind} R^{wake} \left.\frac{\partial V_x}{\partial r}\right|_{R^{wake}} + k_{v_{Shr}} R^{wake}\left\{V_x\left(R^{wake}\right)\right\}\left.\frac{\partial V_x}{\partial r}\right|_{R^{wake}}.$$

From this, $k_{v_{Shr}}$ is expressed by

$$k_{v_{Shr}} = \frac{\int_0^{R^{wake}}\left(V_x\frac{\partial V_x}{\partial x} + V_r\frac{\partial V_x}{\partial r}\right) rdr - k_{v_{Amb}} I_{Amb} V_x^{wind} R^{wake}\left.\frac{\partial V_x}{\partial r}\right|_{R^{wake}}}{R^{wake}\left\{V_x\left(R^{wake}\right)\right\}\left.\frac{\partial V_x}{\partial r}\right|_{R^{wake}}}. \tag{6}$$

In order to avoid the singularity in the expression, the maximum values of k_{vShr} in Eq. (6) is set as 0.1. It is noted that V_x, V_r and R^{wake} at $x = x_{c1}$ (the DWM-inlet) involved in the equation are readily available from the solution of CFD (ALM) in Ω_{NS}. The coefficient, k_{vShr}, determined in this way corresponds to the simultaneous turbine conditions and varies with the time.

As regard to the tangential velocity in the wake flow, there are many experimental studies for helicopters or a wing but only limited studies for wind turbines in literature. A short summary of a survey on the relevant study is given below. Dobrev et al. (2008) studied the wake flow downwind of a three blades turbine experimentally and found that the tangential velocity in the wake may be described by an equation derived by Vatistas (2006) for the wake flow of helicopters, i.e.,

$$V_\theta = V_{\theta\ \max}\frac{r}{r_c}\left[\frac{\alpha+1}{\alpha+(r/r_c)^4}\right]^{(\alpha+1)/4}, \tag{7}$$

where r_c represents the radial position where the maximum tangential velocity occurs, and α is a scaling constant, which is equal to 0.75 for helicopters suggested by Vatistas (2006) but should be smaller than 0.75 for wind turbines suggested by Dobrev et al. (2008). Devenport et al. (1996) presented an experimental study on the tip vortex of a half-wing and suggested the tangential velocity profile induced by a tip vortex may be described by the following equation:

$$V_\theta = V_{\theta\ \max}\left(1+\frac{0.5}{\alpha}\right)\frac{r_c}{r}\left[1-\exp\left(-\alpha\frac{r^2}{{r_c}^2}\right)\right] \tag{8}$$

where $\alpha = 1.25643$. With this value of α, $V_\theta \approx V_{\theta\ \max}$ at $r = r_c$. Inspired by the work of Devenport et al. (1996), we propose that the tangential velocity in the wake of a wind turbine is modelled by

$$V_\theta(x,r)=\begin{cases} V_{\theta\max}(x)\dfrac{r_c}{r}\dfrac{1-\exp(-\lambda r^2/{r_c}^2)}{1-\exp(-\lambda)} & \text{for } r\le r_c \\[2ex] V_{\theta\max}(x)\dfrac{R^{wake}(x)-r_c}{R^{wake}(x)-r}\dfrac{1-\exp\left(-\lambda\dfrac{\left(R^{wake}(x)-r\right)^2}{\left(R^{wake}(x)-r_c\right)^2}\right)}{1-\exp(-\lambda)} & \text{for } r>r_c \end{cases}, \tag{9}$$

where $r^2 = y^2 + z^2$ in the coordinate system used in this paper and the scaling constant λ is assumed to be 1.26 following Devenport et al. (1996). The first part of Eq. (9) is almost the same as Eq. (8) when $\lambda = \alpha \approx 1.26$ but with $\left(1+\frac{0.5}{\alpha}\right)$ replaced by $\frac{1}{1-\exp(-\lambda)}$. This minor change ensures that $V_\theta = V_{\theta\ \max}$ at $r = r_c$ no matter what the value of λ is. This change also opens a door for selecting other values of the scaling constant λ without affecting the satisfaction of condition $V_\theta = V_{\theta\ \max}$ at $r = r_c$, though it is not attempted in this paper. The second part of Eq. (9) is formed by taking the point corresponding to the wake radius ($R^{wake}(x)$) as the vortex centre where the tangential velocity equal to zero.

To use the above equation, it is necessary to determine the values of $V_{\theta\ \max}$ and r_c. Based on our numerical tests, it is assumed that $V_{\theta\ \max}$ linearly varies, i.e.,

$$V_{\theta\ \max}(x) = ax + b \tag{10}$$

where a and b are two coefficients. Our results will show that the coefficients can be determined by using the data just before the DWM inlet. Actually, they are estimated using the maximum tangential velocity from CFD (ALM) at 5 sections between the DWM inlet and the section denoted by the dash-dotted line at $x = x_d$ in Fig. 1. The distance, $x_{c1} - x_d$, is taken as 0.5D. r_c in Eq. (9) is assumed to be evaluated by

$$\frac{r_c}{R^{wake}(x_c)} = \frac{r_{c1}}{R^{wake}(x_{c1})}\beta + (1-\beta) \tag{11}$$

where r_{c1} is the radial coordinate of $V_{\theta\max}$ at the DWM-inlet (x_{c1}), x_c is the axial coordinate of the section where r_c is evaluated. The value of β in Eq. (11) should be $0<\beta<1$. It may be determined in different ways but is proposed to be estimated by

$$\beta = \frac{\frac{r_{c0}}{R} - 1}{\frac{r_{c1}}{R^{wake}(x_{c1})} - 1} \tag{12}$$

where r_{c0}/R is the ratio of the radial coordinate of $V_{\theta\max}$ at the turbine section to the radius of the turbine. Eq. (11) is based on the observation of our numerical tests that shows $r_{c1} \le r_c < R^{wake}$. It is noted that since the values of a, b, β, r_{c1} and $R^{wake}(x_{c1})$ in Eqs. (10)–(12) are simultaneously estimated by using the results obtained by CFD (ALM) in Ω_{NS}, they always correspond to the flow conditions of the turbines which change with time.

The improved dynamic wake model (IDWM) is composed of Eqs. 2–12. The new hybrid method, CFD (ALM)-IDWM, is formed by combining the IDWM with the CFD (ALM) as discussed previously and as shown in Fig. 1. The outlet (i.e., the coupling boundary) of CFD (ALM) is in Ω_{DWM} while the inlet of the IDWM is in Ω_{NS}. The models are coupled together by assigning the velocities of CFD (ALM) to IDWM at the DWM inlet and by assigning the velocities of IDWM to CFD (ALM) at the coupling boundary ($x = x_{c2}$). Mathematically, these can be expressed as

$${}^{DWM}V_x(x_{ci}, r, t) \Leftrightarrow {}^{CFD}V_x(x_{ci}, r, \theta, t), \tag{13a}$$

$${}^{DWM}V_r(x_{ci}, r, t) \Leftrightarrow {}^{CFD}V_r(x_{ci}, r, \theta, t), \tag{13b}$$

$${}^{DWM}V_\theta(x_{ci}, r, t) \Leftrightarrow {}^{CFD}V_\theta(x_{ci}, r, \theta, t), \tag{13c}$$

where $i = 1$ or 2. It is noted that the velocities of IDWM is axisymmetric, i.e., they do not vary with θ while the velocities of CFD (ALM) is generally not axisymmetric. To match them, approximation is required. There may be many options for doing so. In this paper, we just take $\theta = 0$, i.e., just using the velocities of CFD (ALM) on the line of z = 0 and y > 0 in Eq. (11) for $i = 1$ while for $i = 2$, the velocities on the left hand side are assigned to the right hand side at all points with the same values of r. This approach is easy to implement and leads to satisfactory results as discussed below for all the cases considered in this paper. However, it is not perfect and may be replaced by other approaches in future work. Another point worth being discussed is that the IDWM is not solved and applied before the disturbed flow by the turbine reaches the DWM inlet based on the principle of gradual evolution procedure suggested by Jonkman and Shaler (2021). In other words, ${}^{DWM}V_x(x \ge x_{x_{c1}},\ r,\ t) = V^{wind}$, ${}^{DWM}V_r(x \ge x_{x_{c1}}, r, t) = 0$, ${}^{DWM}V_\theta(x \ge x_{x_{c1}}, r, t) = 0$ for $t < x_{c1}/V^{wind}$. Further issue is that there are two values of velocities at any point in the coupling zone for $t \ge x_{c1}/V^{wind}$: one from CFD (ALM) and the other from the dynamic wake model. To smooth them, the following equation suggested by Jacobsen et al. (2011) is applied

$$f(x, r, \theta, t) = f_{CFD}(x, r, \theta, t)\delta + f_{IDWM}(x, r, \theta, t)(1-\delta), \tag{14}$$

where the function, f, can be any one of V_x, V_r, V_θ, δ varies in the range of 0 and 1 according to

$$\delta = 1 - \frac{e^{\varepsilon^{3.5}} - 1}{e - 1}, \tag{15}$$

where e is the Euler's number and $\varepsilon = \frac{x-x_{c1}}{x_{c2}-x_{c1}}$. The two-way coupling of the CFD (ALM) and IDWM is further shown by the flow chart in Fig. 2. It is noted that the time steps used for the two models can be different, but the same steps are employed in this paper. Different approaches may be considered in future work. It is also noted that the two models may be iterated in each of time steps, but the iteration is not performed for the results presented in this paper. Therefore the coupling referred in this paper may be understood as weak two-way coupling.

3. Discussions on the results of CFD (ALM)

The behaviours of the new numerical method - CFD (ALM)-IDWM will be investigated by comparing with the CFD (ALM) model in the next section. Before doing so, the results of CFD (ALM) will be shown to converge for the grids used and are validated against experimental data in this section. On this basis, this section will also discuss some features of the wake obtained by CFD (ALM) to confirm that the assumption of Eq. (10) is reasonable and to provide reference results for discussing the CFD (ALM)-IDWM in the next section.

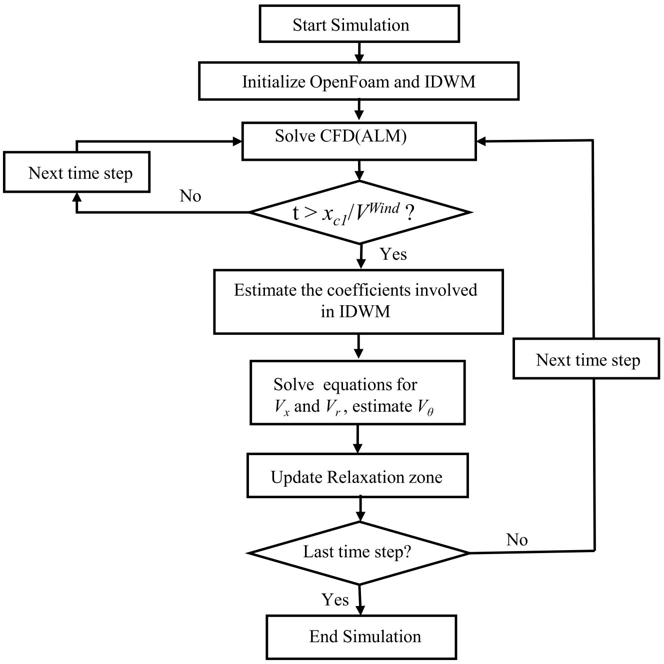

Fig. 2. Flow chart of the CFD (ALM)-IDWM.

For this purpose, the wind turbine model used is the same as that described by Adaramola and Krogstad (2011). The diameter of the turbine is D = 0.894 m and its rotational centre is located z = 0.817 m. More details are given in Table 1. The turbine is supported by a circular tower with varying diameter, which is 0.09 m at its root and 0.05 m at its top.

3.1. Convergent tests and comparison with experimental data

Firstly, the grids to be used for CFD (ALM) are tested. For this purpose, the computational set up is similar to the wind tunnel used by Adaramola and Krogstad (2011), i. e, the length, width and height of domain are taken as L = 11 m, B = 2.7 m and H = 1.9 m, respectively; the unform wind speed at the inlet is applied; zero gradient of the normal velocity and pressure at outlet and non-slip condition on other boundaries are imposed, different from those shown in Fig. 1. The turbine is placed about 2.7 m from the inlet. The wind speed is taken as 10 m/s while the tip speed ratio (TSR) is taken as 6, corresponding to 1200 rpm.

For generating the grids, the domain is split into four regions: A, B, C and D as shown in Fig. 3. The wind turbine is located in Region D. The grid size in Region A is demoted by (dx, dy, dz) in the corresponding direction of x-, y- and z-axes. The grids in Regions B, C, and D are generated in such a way that they have a size of (dx, dy, dz)/2, (dx, dy, dz)/4 and (dx, dy, dz)/8, respectively. Three different grids (denoted by Coarse, Medium and Fine) are considered as detailed in Table 2. A part of one typical grid is illustrated in Fig. 3. The time step, Δt, chosen corresponds to 1° angular displacement of the turbine, i.e., the average Courant number being less than 1. For all the cases, more than 100 turbine rotations are calculated to ensure that the turbine aerodynamics became relatively stable.

Table 1
The basic properties of the turbines.

Airfoil	S826
Number of blades	3
Rotor diameter(m)	0.894
Hub diameter(m)	0.13
Hub height(m)	0.817

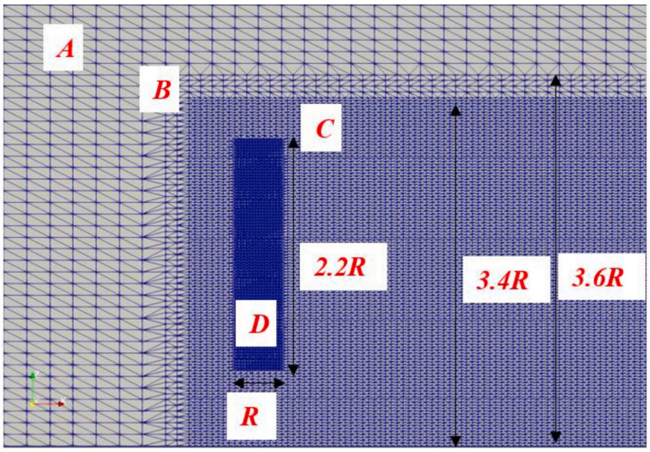

(a) Side view

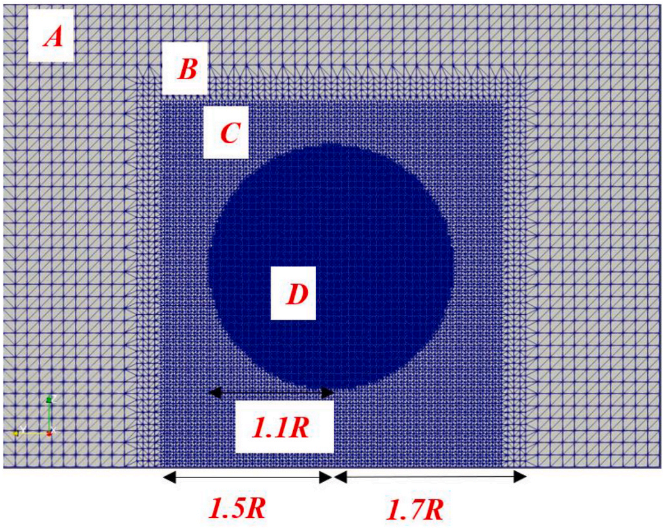

(b) Front view

Fig. 3. Illustration of grids (*R*: diameter of the turbine). The turbine is included in Region D where the grid is the finest. The grid sizes from Region D to Region A increase by a factor of 2.

Table 2
Mesh generation scheme.

Grid name	Mesh	L/dx	H/dz	B/dy	Total mesh (million)
G1	Coarse	78	27	38	1.63
G2	Medium	110	38	54	4.47
G3	Fine	154	53	75	12.26

Fig. 4 shows the time histories of power and thrust coefficients corresponding to all grids. It can be seen that the mean values and the oscillating amplitudes of the coefficients for the medium (G2) and fine (G3) grids are almost the same, while these for the coarse grid are visibly different. The relative differences in the mean value of Cp and C_T for G2 from these for G3 are 0.1% and 0.15%, respectively, while the corresponding differences for G1 are 1% and 2%.

Fig. 5 shows the axial velocity profiles at two locations behind the turbine together with the experimental data from Adaramola and Krogstad (2011). The relative errors of the numerical results for different grids to the experimental data are calculated by using

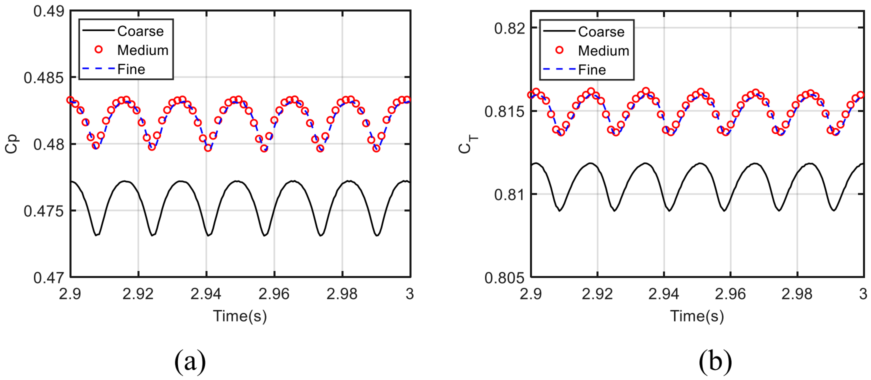

Fig. 4. The time histories of power and thrust coefficients for V^{Wind} = 10 m/s and TSR = 6: (a) power coefficient (C_P), (b): thrust coefficient (C_T).

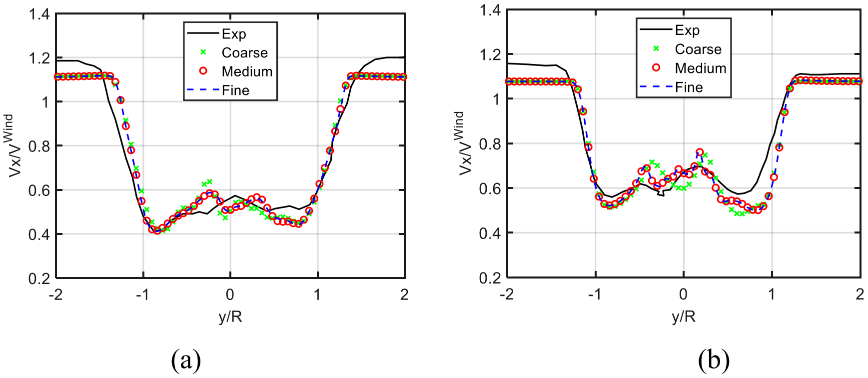

Fig. 5. Axial velocity profiles averaged over 80th-100th rotations at z = 0.817 m for V^{Wind} = 10 m/s and TSR = 6 (a): Vx/V^{Wind} at x = 1D, (b): Vx/V^{Wind} at x = 3D.

$$Error2 = \frac{1}{n}\frac{\sum_{i=1}^{n}\left|\overline{V}_{CFD(ALM)}(y_i) - \overline{V}_e(y_i)\right|}{\sum_{i=1}^{n}\left|\overline{V}_{CFD(ALM)}(y_i)\right|}, \tag{16}$$

where $\overline{V} = \widetilde{V}_x / V^{wind}$ with $\widetilde{V}_x$ being the averaged axial velocity over the 80th-100th rotations of the turbine at a spatial point, and $\overline{V}_e(r_i)$ is the experimental data while these with subscripts of *CFD(ALM)* are the numerical results. These are all taken from Fig. 5. The relative errors are shown in Fig. 6. Again, not much difference between the results of G2 and G3 is observed. Apart from this, the relative error from G1 to G2 changes considerably but does not change significantly from G2 to G3, indicating convergence of the numerical results. The numerical velocity profiles are similar to the experimental data, though their relative errors are at the level of about 6–9%.

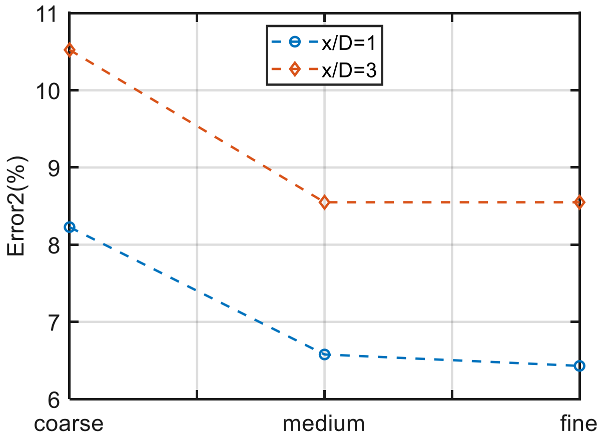

Fig. 6. Relative errors of numerical axial velocity profiles averaged over 80th-100th rotations to the experimental data (The results in Fig. 5 are used for calculating the relative errors.).

The numerical results of mean power and thrust coefficients are further compared with the experimental data for a range of TSR values in Fig. 7. In addition to ours, some results denoted by 'Manger' from Krogstad and Eriksen (2013) are also plotted in the figure, which were obtained by running Ansys Fluent with k-ω SST turbulent model and with the blade geometry resolved. The overall agreement between the present numerical results and experimental data is acceptable. More specifically, at the design value of TSR, the numerical power coefficients are slightly larger than the measured value; at other TSR values, the CFD (ALM) results are smaller while the results from Krogstad and Eriksen (2013) are larger at the smaller TSR but smaller at the larger TSR. For the thrust coefficients, our results are very similar to those of Krogstad and Eriksen (2013). Both have similar trends to the experimental data but are visibly smaller than the experimental ones.

This subsection indicates that the results of the CFD (ALM) are satisfactory compared with experimental results, and that the grid similar to G2 is appropriate. All the grids used for the results presented below are similar to G2.

3.2. *Some features of wake flow*

In this subsection, we will present some results obtained by using CFD (ALM) to reveal some features of wake flow. These features will confirm our assumption used for Eq. (10), and will provide evidence for

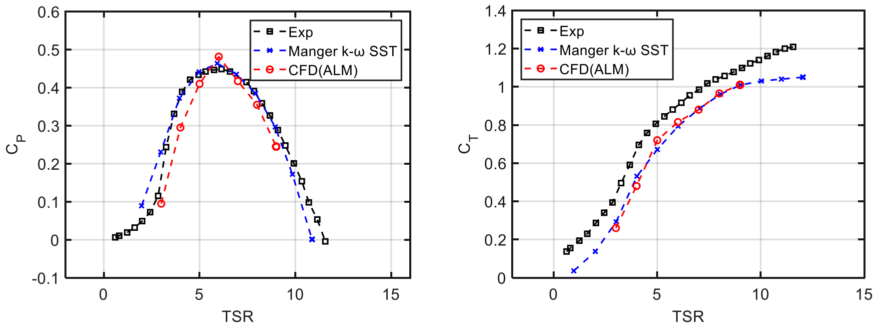

(a)

(b)

Fig. 7. Comparison of mean numerical power and thrust coefficients with experimental data for different TSR with $V^{Wind} = 10$ m/s. (a) Power coefficient, (b) Thrust coefficient.

discussing the results in the following section.

For this purpose, the same turbine as in the above section is considered but the domain is enlarged to reduce the block effects of artificially boundaries. The length, width and the height of the computational domain are 17*D,* 4.5D and 4.5D, respectively. The boundary conditions are the same as illustrated in Fig. 1. The grids used is similar to G2 described above. The wind speed is 10 m/s and TSR will take different values.

Fig. 8 shows the profiles of the tangential velocity (denoted by V_z) at the points on the line of -2 R < y < 2 R and z = 0.817 m at different axial locations after the turbine (1D, 3D … … representing x = 1D, 3D ……). The results are obtained by averaging the corresponding velocities over 80th-100th turbine rotations for TSR = 6. One can see that the maximum value of the tangential velocity gradually decreases with the increase of the distance from the turbine. To further show this feature, Fig. 9 plots the maximum of the tangential velocity at different locations for a range of TSR. It can be seen that the maximum almost linearly varies from about $x/D = 2$ for all the cases. If the location where the maximum tangential velocity become linearly varying is denoted by X_L, we have $X_L \approx 2D$ for these cases. More interesting thing is that the linear fitting lines obtained only by using the numerical data in the region between the coupling boundary and the section of X_L can well fit all the data downwind. This does not only confirm that the assumption used for Eq. (10) is reasonable but also indicates that the constants, *a* and *b,* in Eq. (10) can be determined by using the data in the region before coupling boundary and after the section demoted by X_L. It is noted that the value of X_L is not very sensitive to the grids based on our numerical tests (not presented here), and so it may be estimated by preliminary tests using a course grid.

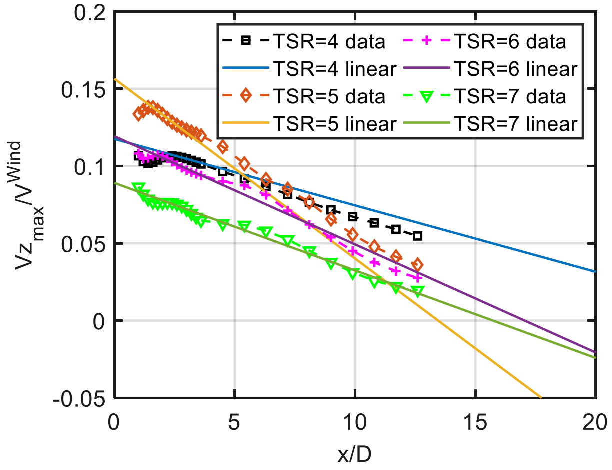

Fig. 9. Variation of the maximum of averaged tangential velocity over 80th-100th rotation on the line of $\theta = 0$ along the axial direction for $V^{Wind} = 10$ m/s (points denote the results obtained by CFD (ALM); the lines with ‘linear’ being the fitting lines obtained by using the data of CFD (ALM) between the section of X_L and the coupling boundary).

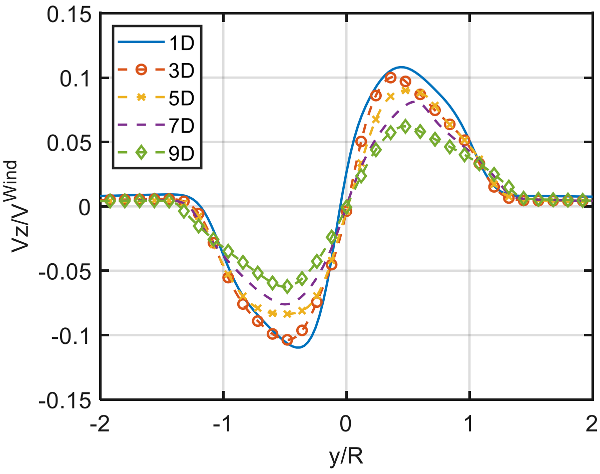

Fig. 8. Profiles of tangential velocity (V_z) averaged over 80th-100th rotations along a horizontal line (-2 R < y < 2 R, z = 0.817 m) for $V^{Wind} = 10$ m/s and TSR = 6.

Another feature to be discussed is about the variation of the axial velocity in the wake. For the same case as in Fig. 8, the profiles of the axial velocity averaged over 80th-100th rotations along a horizontal line (-2 R < y < 2 R,z = 0.817 m) at different axial locations is depicted in Fig. 10. At each of the locations, there is a minimum velocity, e.g., $V_x/V^{Wind} \approx 0.4$ at $x/D = 3$. It varies with the axial locations. It decreases from $V_x/V^{Wind} \approx 0.5$ at $x/D = 1$ to $V_x/V^{Wind} \approx 0.4$ at $x/D = 3$, before it increases. The recovery of the axial velocity in the far wake is a well-known phenomenon. What we are more interested here is where the smallest minimum velocity occurs and how it is affected by the rotational speeds. To reveal more, Fig. 11 plots the minimum axial velocity for a range of TSR values. For each value of TSR, there is a smallest minimum and a location, p_0, corresponding to it. P_0 varies between $x/D = 2$ and $x/D = 4$ in the cases. For example, p_0 occurs at $x/D = 2.8$ for TSR = 6. Later we will demonstrate that the coupling boundary for CFD (ALM)-IDWM should be chosen after p_0 to produce better prediction of the wake flow properties.

As it affects the choice of the coupling boundary for CFD (ALM)-IDWM, it is worth studying how sensitive p_0 is to the computing set up.

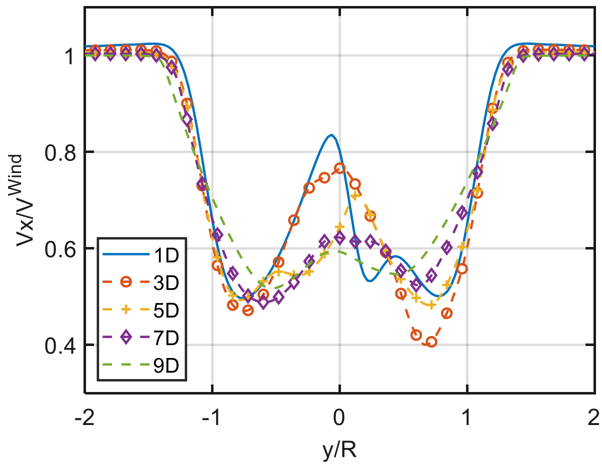

Fig. 10. Profiles of axial velocity averaged over 80th–100th rotations along a horizontal line (-2 R < y < 2 R,z = 0.817 m) for V^{Wind} = 10 m/s and TSR = 6.

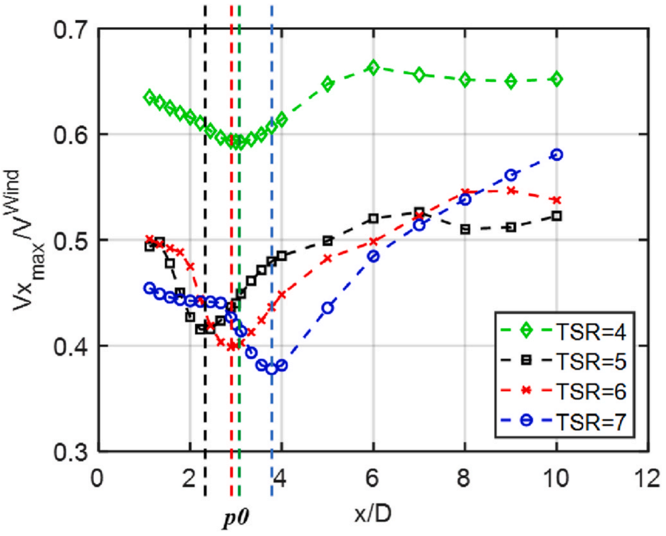

Fig. 11. Minimum axial velocity at different sections calculated by using CFD (ALM) for V^{Wind} = 10 m/s.

For this purpose, we recalculate the case with TSR = 6 by using different grids, similar to G1, G2 and G3 in Table 2 and place the outlet at $x/D = 4$. For different cases, the location of p_0 varies in the range of 2.5D-3.8D, roughly same as in Fig. 9. This indicates that this location is not very sensitive to the setting up, and that it can be estimated by preliminary tests with coarse grids and smaller computational domain.

4. Behaviours of the new hybrid method - CFD (ALM)-IDWM

The key elements involved in the new hybrid method is the coupling of the two models and the improved dynamic wake models as discussed in the previous sections. Regarding the coupling, the important aspect is where the coupling boundary should be located. In this section, we will discuss the effects of the coupling boundary location and the performance of the improved dynamic wake model by comparing the results of the new method with the full CFD simulation in the whole computational domain. The results to be presented and discussed include these (wind power, thrust and velocity profiles) in the near wake and these (velocities) in the far wake.

4.1. Effects of the coupling boundary locations

One of issues related to CFD (ALM)-IDWM is how to select the coupling boundary location and how the location of the coupling boundary affects the numerical results. This subsection will discuss this issue. For this purpose, the turbine model and computational domain are chosen as the same as those for Fig. 8 unless described otherwise. The length of the domain (Ω_{DWM}) for the dynamic wake model varies depending on where the coupling boundary is located. The grid for the domain of Ω_{NS} is similar to G2. The domain of Ω_{DWM} is split by dx = D/9 in axial direction and dr = D/32 in radial direction.

Fig. 12 presents the time histories of power and thrust coefficients obtained by using CFD (ALM) in the whole computational domain (i.e., with its outlet set at x = 13D) and by the CFD (ALM)-IDWM with its coupling boundary at x = 2D, 3D or 4D. From this figure, we can see that the aerodynamic coefficients obtained by the CFD (ALM)-IDWM with different locations of the coupling boundary are almost the same, and also that they agree very well with these obtained by CFD (ALM). The largest error occurs when the coupling boundary is at x = 2D, which is about 0.5% for power coefficient and 0.1% for thrust coefficient.

Fig. 13 plots the axial velocity profiles averaged over 80th-100th rotations at two axial locations in the near wake for the same cases of Fig. 12. It shows that the velocities obtained by CFD (ALM)-IDWM with different coupling boundary locations have not much visible differences between them and from these obtained by CFD (ALM).

To further reveal the sensitivity of the results to the different locations of the coupling boundary, the errors of the axial velocity profiles at x = 1.5D obtained by CFD (ALM)-IDWM with its coupling boundary at x/D = 2, 3 …. 13 are estimated. The velocities are these recorded at 100th rotations. The errors are calculated by using a similar equation to Eq. (16) but $\overline{V}_e$ is replaced by the axial velocity calculated by using CFD (ALM) in the whole computational domain (i.e., these denoted by CFD (ALM) in the figure) while $\overline{V}_{CFD(ALM)}$ by these from CFD (ALM)-IDWM (i.e., these denoted by CFD (ALM)-IDWM in the figure). The resulted errors are plotted in Fig. 14. In addition, the similar error of CFD (ALM) with its outlet at x/D = 2, 3, …13, respectively, are also plotted in this figure. It can be seen that the errors of CFD (ALM)-IDWM are very small, less than 0.6%, for different locations of the coupling boundary. The errors of CFD (ALM) with its outlet at a location near the turbine are considerable larger than these of CFD (ALM)-IDWM, though they all would be acceptable from engineering point of view.

Figs. 12–14 tell us that the dependence of the aerodynamic coefficients and the velocity at the near wake on the location of the coupling boundary is very weak.

However, the story for the velocities in the wake further downwind is different. Fig. 15 presents the errors, calculated in the same way as Fig. 14, of axial velocity taken at different sections for TSR = 4,5,6 and 7. The velocities are estimated by using CFD (ALM)-IDWM with its coupling boundary at x=(p_0-1D)+0.5D, p_0+0.5D or (p_0+1D)+0.5D, where p_0 represents the location of the smallest minimum axial velocity discussed in Fig. 11; p_0-1D, p_0 and p_0+1D represent the location of the inlet boundary of IDWM. One can see that there is no significant difference between these obtained by using p_0 and p_0+1D as the inlet boundary of IDWM or using p_0+0.5D and (p_0+1D)+0.5D as the location of the coupling boundary. However if the p_0-1D is used as the location of the inlet boundary of IDWM or (p_0-1D)+0.5D as the location of coupling boundary, the error is considerable larger, though it still less than 6%. In addition, the errors in this figure are much higher than those in Fig. 14. That is because the velocities at the locations of x > 4D are estimated by using the improved dynamic model which is based on a number of assumptions as discussed previously and so larger errors are expected. Nevertheless, the errors are less than 5% when proper location of the coupling boundary is used and are acceptable from the engineering point of view.

Based on the results in Fig. 15, the location of the coupling boundary

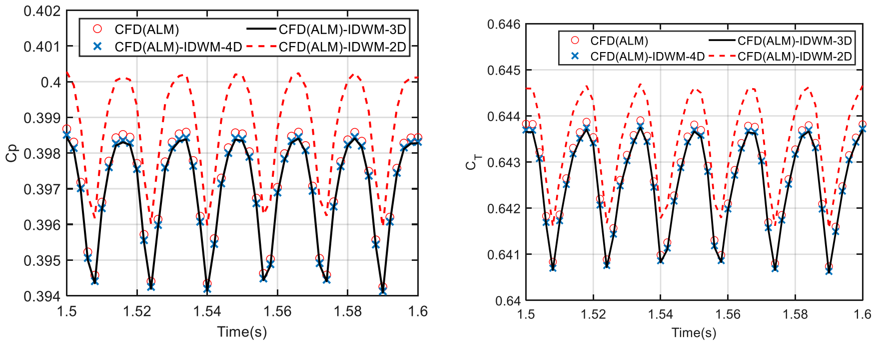

(a) Power coefficient (b) Thrust coefficient

Fig. 12. Comparison of time histories of power and thrust coefficients for TSR = 6 and V^{Wind} = 10 m/s obtained by CFD (ALM) and CFD (ALM)-IDWM (2D, 3D and 4D indicating that the coupling boundary is located at x = 2D, 3D and 4D, respectively).

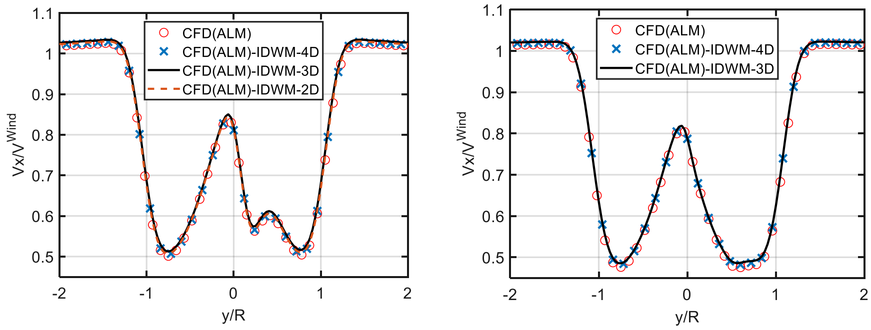

(a) (b)

Fig. 13. Comparison of axial velocity profiles averaged over 80th–100th rotation, taken on the line of -2 R < y < 2 R,z = 0.817 m and (a) $x = 1D$ and (b) $x = 2D$.

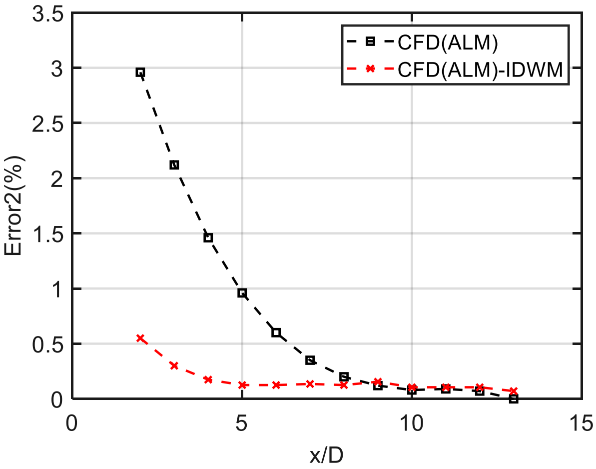

Fig. 14. Error of axial velocity taken at x = 1.5D for TSR = 6 and V^{Wind} = 10 m/s.

should be selected to be downwind of p_0 to obtain better results for the wake flow. However another factor should be considered when selecting the location, i.e. whether the maximum tangential velocity follows the linear trend as discussed in Fig. 8. Clearly if the coupling boundary is too close to the turbine, the maximum tangential velocity will not vary linearly and so Eq. (10) is not valid. Considering the two aspects, the location of the coupling boundary x_{c2} would be taken as x_{c2} = max (p_0 + 0.5D, X_L). The problem is that we do not know X_L and p_0 beforehand, which come from the result of CFD (ALM). This problem may be resolved in two ways. One is to estimate them based on empirical data. The other is to estimate them by preliminarily running CFD (ALM) with a coarse grid and smaller computational domain. As discussed before, this can produce the good estimates to p_0 and X_L. However it should be noted that we may still obtain quite good results for the wake flow even p_0 and X_L are not very accurate based on our numerical tests so far and as shown in Fig. 15.

4.2. *Performance of the improved dynamic wake model*

One of main contributions of this paper is to develop an improved dynamics wake model used for CFD (ALM)-IDWM as described in Section 2.5. Some results will be presented to demonstrate the effectiveness of the new model. For the purpose of this section, the turbine model is the same as in previous sections. The computational setup is similar to Fig. 15 unless mentioned otherwise. The location of the coupling boundaries is selected to be x_{c2} = 3.6D, 2.5D, 3.4D, 4.3D for TSR = 4,5,6,7, respectively, based on the numerical tests discussed for Figs. 9 and 15. For comparison, the cases are also simulated by using CFD (ALM)-DWM, which is based on the dynamic wake model currently used in literature as discussed in Section 4, and by using CFD (ALM) in the whole computational domain. The location of the coupling boundary for CFD (ALM)-DWM is the same as for CFD (ALM)-IDWM. Table 3 shows the results of the mean power and thrust coefficients obtained by using three different methods. Overall, the difference between the results are insignificant, though the difference of the results obtained by CFD (ALM)-DWM from these of CFD (ALM) is slightly larger than the

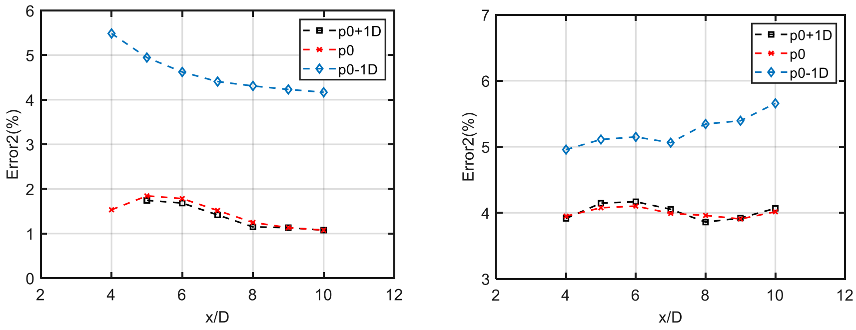

(a) TSR=4

(b) TSR=5

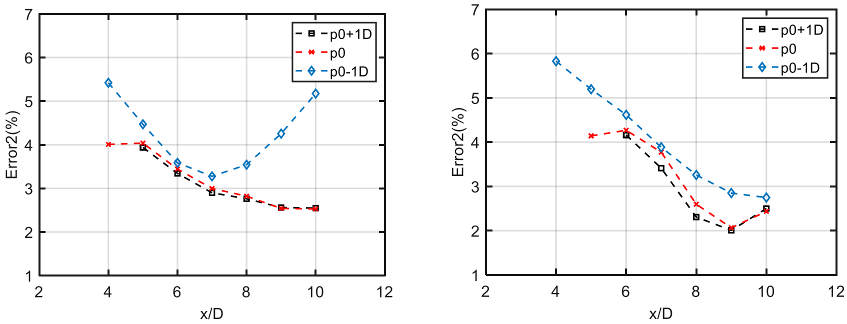

(c) TSR=6

(d) TSR=7

Fig. 15. Error of the axial velocity profiles obtained by CFD (ALM)-IDWM with different location of the coupling boundary. The velocities are these obtained at 100th rotations. p_0-1D, p_0-1D and p_0+1D represent the location of the inlet boundary of IDWM.

Table 3
Mean aerodynamic coefficients.

TSR	CFD (ALM)/CFD (ALM)-IDWM/CFD (ALM)-DWM			
	4	5	6	7
Cp	0.239/0.240/ 0.231	0.375/0.375/ 0.390	0.397/0.396/ 0.404	0.375/0.376/ 0.363
C_T	0.372/0.372/ 0.368	0.485/0.485/ 0.492	0.642/0.642/ 0.648	0.683/0.684/ 0.679

difference of the results obtained by CFD (ALM)-IDWM. Specifically, the maximum error of the results of CFD (ALM)-IDWM compared to CFD (ALM) is less than 0.7% while the maximum error of CFD (ALM)-DWM is about 4%.

Fig. 16 presents the dynamic pressure distribution along a line of -2 R < y < 2 R, z = 0.817 m, taken at two axial locations, x = 1D and 2D, for different values of TSR. One can see that there is not much visible difference between the pressure obtained by CFD (ALM)-IDWM and CFD (ALM). The differences in the results of CFD (ALM)-DWM from those of CFD (ALM) are also insignificant, though they are slightly larger.

Fig. 17 depicts the tangential velocity profiles averaged over 80^{th}-100^{th} rotations along the horizontal line of -2 R < y < 2 R and z = 0.817 m, taken at x = 1D, 2D and 3D, normalized by the incoming wind speed. Again there is no much difference in the results of CFD (ALM)-IDWM from these of CFD (ALM). The results of CFD (ALM)-DWM are also very close to those of CFD (ALM) but have visible difference, particularly at the location near the coupling boundary.

Fig. 18 plots the distribution of deficit velocity averaged over 80^{th}-100^{th} rotations along the horizontal line of -2 R < y < 2 R and z = 0.817 m, taken at x = 1D, 2D and 3D, respectively, normalized by the incoming wind speed. The deficit velocity is calculated by $|\overrightarrow{u}^{wake}| = \sqrt{(V_x^{wake})^2 + V_r^2 + V_\theta^2}$. The similar agreement between the results to that of Fig. 17 is observed.

All the results shown in Figs. 16–18 and Table 3 demonstrate that use of both the existing dynamic wake model and the improved dynamics model for coupling with CFD (ALM) can give quite good results for the aerodynamics coefficients and for the wake flow near the turbine before the coupling boundary.

However, the observation is different for the wake flow after the coupling boundary. This can be seen in Figs. 19–22 for the same cases for Figs. 15–17. One aspect is that CFD (ALM)-DWM) ignores the tangential velocity in the far wake but the results of CFD (ALM) and CFD (ALM)-IDWM indicated that the tangential velocity magnitude can be about 1/10 of the wind speed as shown in Fig. 19. This figure also shows that the tangential velocity is well modelled by the improved dynamic wake model.

Fig. 20 presents the distribution of deficit velocity averaged over 80^{th}-100^{th} rotations along the horizontal line of -2 R < y < 2 R and z = 0.817 m, taken at x = 4D, 6D, 8D and 10D, respectively, non-dimensionalized by the incoming wind speed. As can be seen, in the far field, the deficit velocity profiles have a local minimum near the centre of the wake and two local maxima from the results of CFD (ALM). CFD (ALM)-IDWM can catch the feature well and produce quite good results agreeing well with CFD (ALM). However, CFD (ALM)-DWM can fail to catch the feature, and its results are quite different from these of CFD (ALM).

This is further illustrated by Fig. 21, which shows the streamlines starting from a circular surface with a radius of 1 R at $x/D = 4$ at 100^{th} rotations for TSR = 6 based on the results obtained by using the three methods. One can see that the streamlines from CFD (ALM) and CFD (ALM)-IDWM are spiral while they are almost straight from the results of CFD (ALM)-DWM. This is further illustrated by a surface formed by the streamlines starting from the line of -1.5 R < y < 1.5 R, z = 0.817 m and

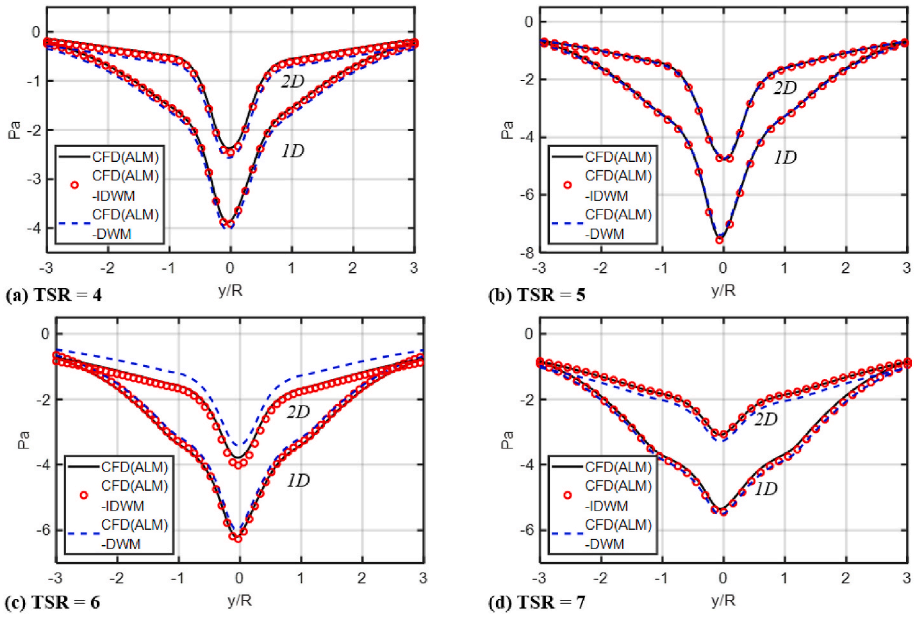

(a) TSR = 4 (b) TSR = 5 (c) TSR = 6 (d) TSR = 7

Fig. 16. Near-field dynamic pressure averaged over 80th–100th rotation along the horizontal line -2 R < y < 2 R, z = 0.817 m for TSR = 4,5,6 and 7.

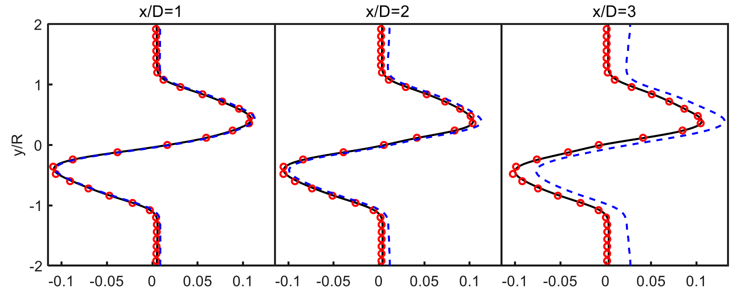

(a) TSR=4

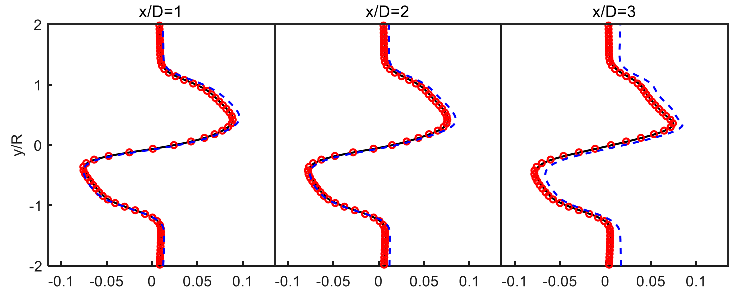

(b) TSR =7

Fig. 17. Tangential velocity profiles (normalized by V^{wind}) averaged over 80th-100th rotation along the horizontal line of -2 R < y < 2 R and z = 0.817 m for TSR = 4 and 7 (solid line: CFD (ALM); circles: CFD (ALM)-IDWM; dashed line: CFD (ALM)-DWM; the unit for velocity is meter).

$x/\mathrm{D} = 4$ in Fig. 22. The streamline surface of CFD (ALM) and CFD (ALM)-IDWM are curling while it is just a plane surface for CFD (ALM)-DWM. The phenomena are consistent with the fact in Fig. 19 that the tangential velocities from CFD (ALM) and CFD (ALM)-IDWM is considerable while they are zero for CFD (ALM)-DWM.

All the results in Figs. 19–22 demonstrated that CFD (ALM)-IDWM with the improved dynamic wake model can produce a quite good wake flow in the far wake while the CFD (ALM) -DWM with the existing dynamic wake model cannot catch the main features of the far wake flow.

4.3. *Computational efficiency of CFD (ALM)-IDWM*

It is mentioned before that the main reason to develop the new hybrid method is to improve the computational efficiency for estimating the far wake flow. The reasoning for achieving is obvious as the computational time used by IDWM is much smaller than that used by CFD (ALM). This section will give some quantitative information about how much computational time would be saved if CFD (ALM)-IDWM is used.

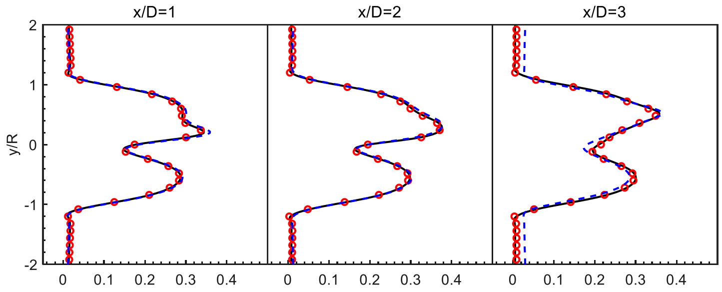

(a)TSR=4

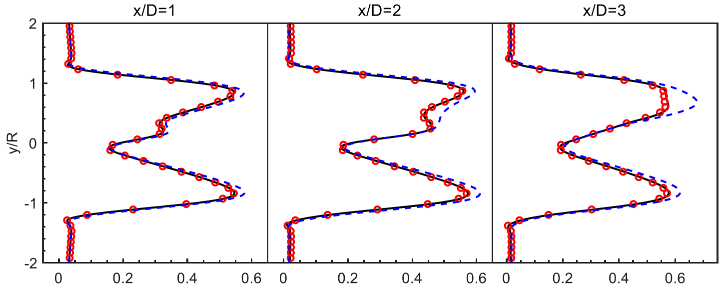

(b) TSR=7

Fig. 18. Deficit velocity profiles $(|\vec{u}^{wake}|/V_x^{Wind})$ averaged over 80th-100th rotation along the horizontal line of -2 R < y < 2 R and z = 0.817 m for TSR = 4 and 7 (solid line: CFD (ALM); circles: CFD (ALM)-IDWM; dashed line: CFD (ALM)-DWM).

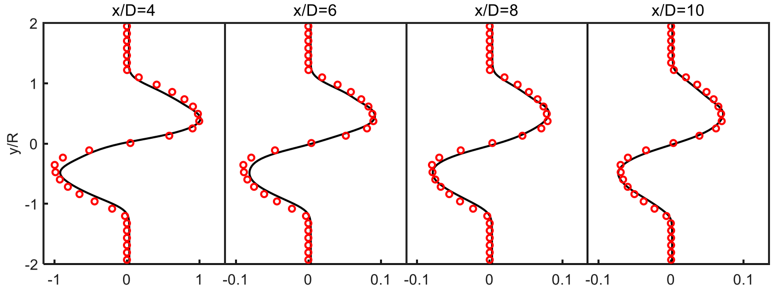

(a) TSR=4

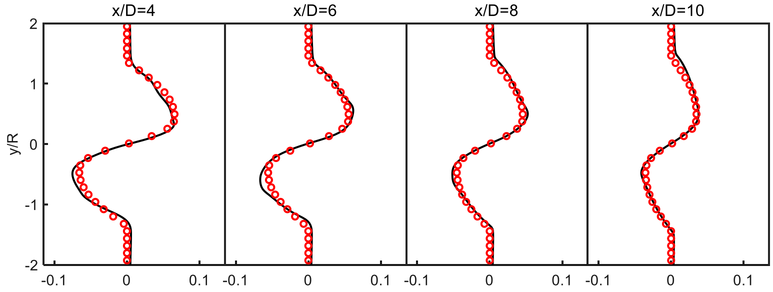

(b) TSR=7

Fig. 19. Tangential velocity profiles (normalized by V^{wind}) averaged over 80th-100th rotation along the horizontal line of -2 R < y < 2 R and z = 0.817 m for TSR = 4 and 7, taken at different axial locations (solid line: CFD (ALM); circles: CFD (ALM)-IDWM).

For this purpose, the same cases as for these described in Section 4.2 will be considered. All cases are run on a workstation with Intel (R) Xeon (R) CPU E5-2660 v3@2.60 GHz 24 core processor for 100 rotations of the turbine. To achieve the results presented in the previous section, the computational time used by the three methods are presented in Fig. 23. As can be seen, for all the case, the computational time used by CFD (ALM)-IDWM is about 47%–57% of that used by CFD (ALM). The computational time used by CFD (ALM)-DWM is similar to that CFD (ALM)-IDWM, though it is slightly less. Specific values depend on the specific cases. Of course, the results in this figure may be different for other cases not considered in the paper, and depends on the computational setup, in particular the length of the domain covered by the

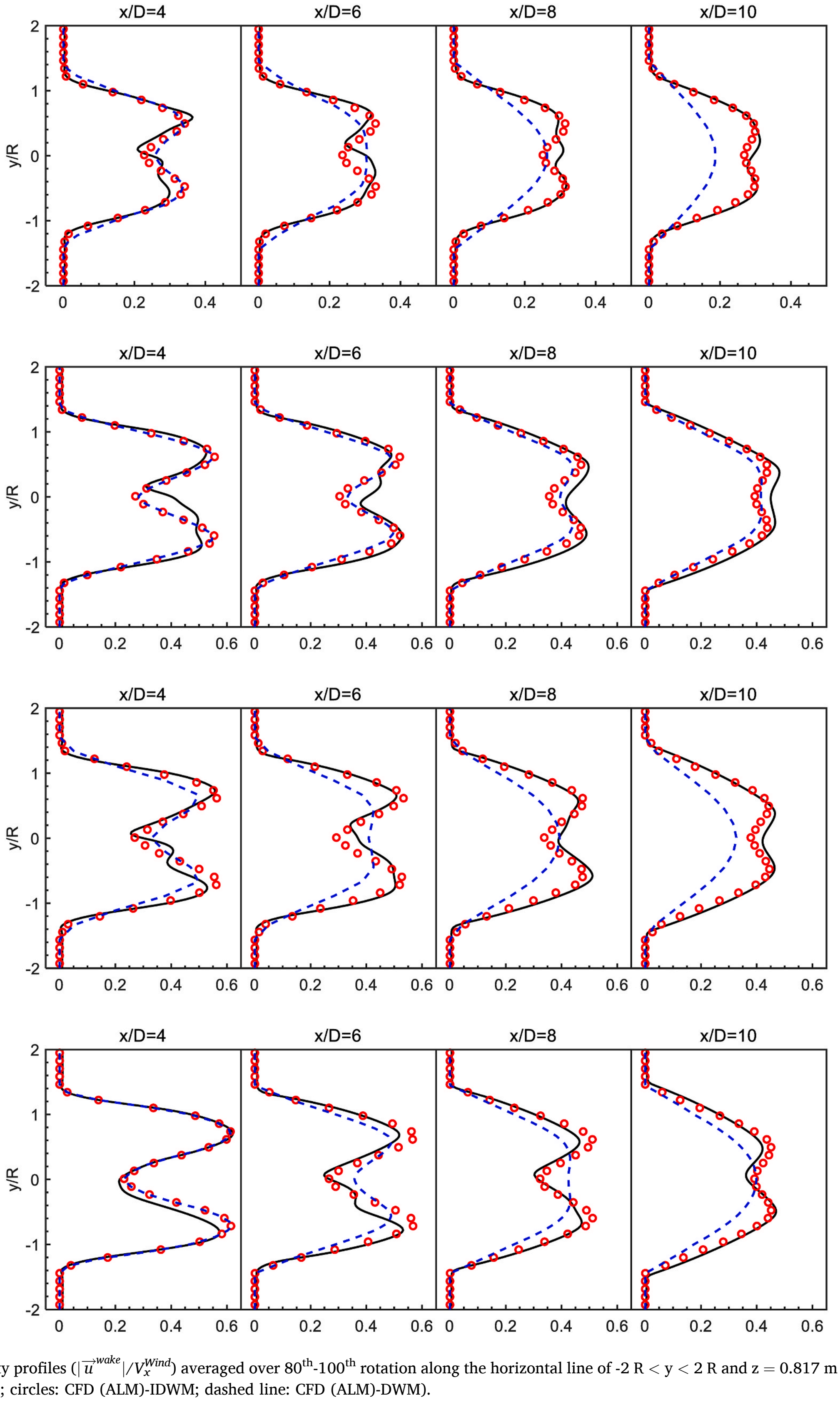

Fig. 20. Deficit velocity profiles ($|\overrightarrow{u}^{wake}|/V_x^{Wind}$) averaged over 80th-100th rotation along the horizontal line of -2 R < y < 2 R and z = 0.817 m for TSR = 4,5,6 and 7 (solid line: CFD (ALM); circles: CFD (ALM)-IDWM; dashed line: CFD (ALM)-DWM).

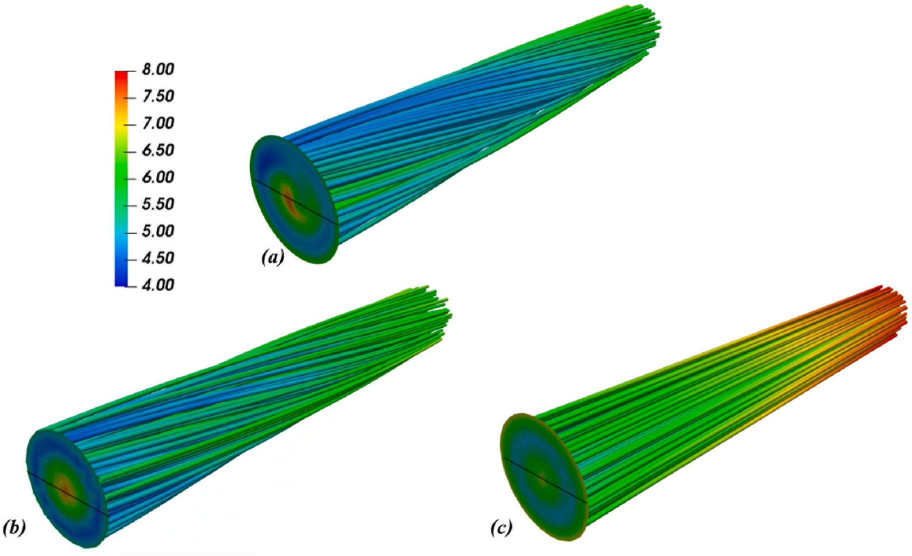

Fig. 21. Streamlines starting from a circular surface with a radius of 1 R at x/D = 4 at 100th rotations for TSR = 6: (a) CFD (ALM), (b) CFD (ALM) -IDWM, (c)CFD (ALM)-DWM (color represents total velocity magnitude).

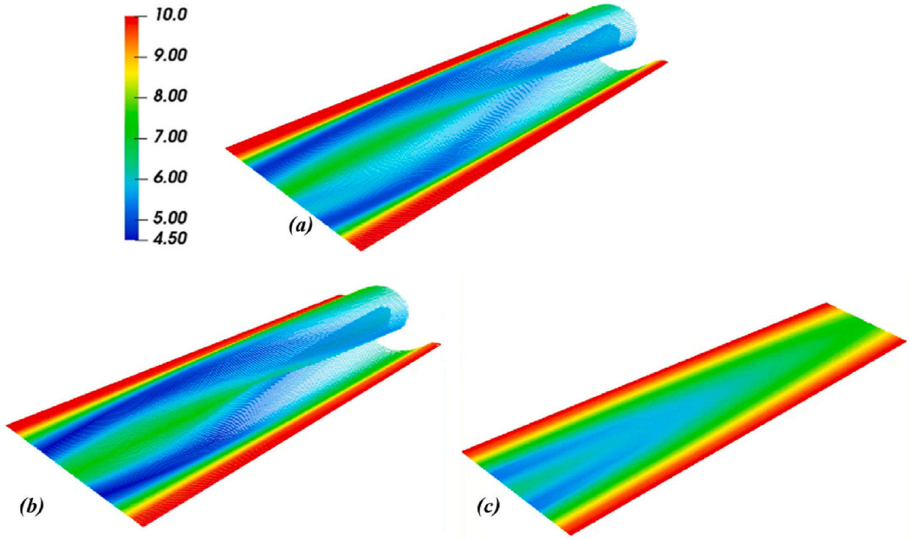

Fig. 22. A surface formed by all the streamlines starting from a line between −1.5 R < y < 1.5 R, z = 0.817 m at x/D = 4 at 100th rotations for TSR = 6: (a) CFD (ALM) (b) CFD (ALM) -IDWM (c)CFD (ALM)-DWM (color represents the size of total velocity magnitude).

dynamic wake model. But it can be understood that the longer of the domain for the dynamic model, the more CUP time is saved by using the hybrid method.

5. Summary and conclusions

This paper presents a new hybrid method for modelling offshore wind turbines and its wakes. The method is named as CFD (ALM)-IDWM. In the method, the near wake flow is simulated by a CFD model based on full Navier–Stokes (NS) equations with the turbine represented by actuator lines while the far wake is modelled by an improved dynamic wake model based on the equations obtained by simplifying the NS equations. The two models are two-way coupled in the coupling zone downwind the turbine. The dynamic wake model (i.e., IDWM) employed in the hybrid method is obtained by improving the existing model in two aspects. (1) The coefficient ($k_{v_{Shr}}$) is estimated simultaneously by using the CFD numerical results, which does not only reduce the uncertainties due to artificial specification of $k_{v_{Shr}}$ but also make the model better consistent with the flow near the turbine, compared to that used in the existing DWM. (2) The tangential velocity ignored in the existing DWM is taken into account by proposing a new model, and the coefficients involved in the model are also simultaneously estimated by the CFD numerical results.

The newly formulated hybrid method is validated by the results from the full CFD simulations in the whole computational domain under different conditions. It is demonstrated that the new hybrid method can produce the numerical results very close to those of full CFD simulations, not only in the near wake (wind power, thrust and velocity profiles) but also in the far wake (axial or total and tangential velocities). It is also demonstrated that the use of IDWM leads to much better results of the velocities in the far wake than use of the existing dynamic wake model. More important is that the hybrid method take much less computational time (around 50% in the case considered) than that taken by the full CFD simulation to achieve the similar results.

This is the first paper to present the new method. Only preliminary tests are carried out on the new method. Future work will apply this

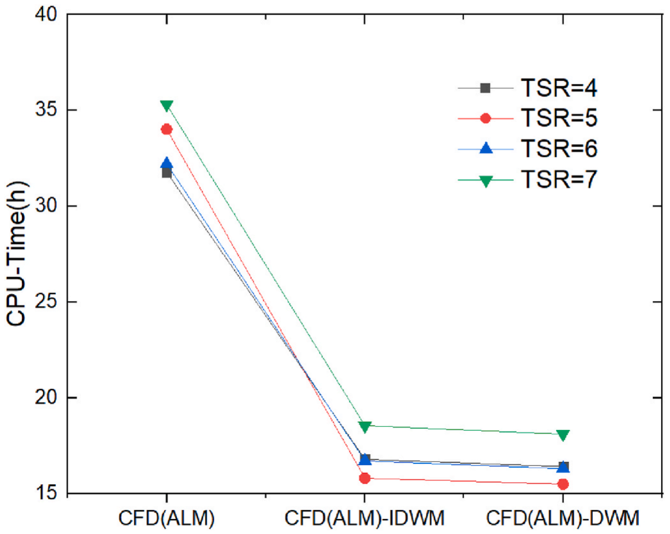

Fig. 23. Comparison of computational time used by CFD (ALM), CFD (ALM)-IDWM and CFD (ALM)-DWM.

method to more complex cases, such as those with clear wake deflection phenomenon, multiple turbines, floating wind turbines, and so on.

CRediT authorship contribution statement

Yuming Yuan: Methodology, Writing – original draft. **Q.W. Ma:** Methodology, Conceptualization, Formal analysis, Writing - review & editing. **Shiqiang Yan:** Methodology. **Xing Zheng:** Supervision. **Kangping Liao:** Supervision. **Gang Ma:** Supervision. **Hanbing Sun:** Supervision. **Abbas Khayyer:** Writing - review & editing.

Declaration of competing interest

The authors declare that they have no known competing financial interests or personal relationships that could have appeared to influence the work reported in this paper.

Data availability

Data will be made available on request.

Acknowledgments

The authors from Harbin Engineering would like to acknowledge the National Natural Science Foundation of China (51739001, 51879051), China. The authors from City, University of London gratefully acknowledge the financial support of EPSRC (EP/T00424×/1, EP/V040235/1), UK. A part of the research related to this paper was carried out when the first author was a visiting student at City, University of London under the support of CSC studentship.

References

Adaramola, M.S., Krogstad, P.A., 2011. Experimental investigation of wake effects on wind turbine performance. Renew. Energy 36 (8), 2078–2086. https://doi.org/10.1016/j.renene.2011.01.024.

Ainslie, J.F., 1988. Calculating the flow field in the wake of wind turbines. J. Wind Eng. Ind. Aerod. 27, 213–224. https://doi.org/10.1016/0167-6105(88)90037-2.

Archer, C.L., Vasel-Be-Hagh, A., Yan, C., Wu, S., Pan, Y., Brodie, J.F., Maguire, A.E., 2018. Review and evaluation of wake loss models for wind energy applications. Appl. Energy 226, 1187–1207. https://doi.org/10.1016/j.apenergy.2018.05.085.

Bastankhah, M., Porté-Agel, F., 2014. A new analytical model for wind-turbine wakes. Renew. Energy 70 (1), 116–123. https://doi.org/10.1016/j.renene.2014.01.002.

Calaf, M., Meneveau, C., Meyers, J., 2010. Large eddy simulation study of fully developed wind-turbine array boundary layers. Phys. Fluids 22 (1), 015110. https://doi.org/10.1063/1.3291077.

Devenport, W.J., Rife, M.C., Liapis, S.I., Follin, G.J., 1996. The structure and development of a wing-tip vortex. J. Fluid Mech. 312, 67–106. https://doi.org/10.1017/S0022112096001929.

Dobrev, I., Maalouf, B., Troldborg, N., Massouh, F., 2008. Investigation of the Wind Turbine Vortex Structure. 14th Int Symp on Applications of Laser Techniques to Fluid Mechanics. Lisbon 2008.

Frandsen, S.T., Barthelmie, R.J., Pryor, S.C., Rathmann, O., Larsen, S.E., Højstrup, J., Thøgersen, M., 2006. Analytical modelling of wind speed deficit in large offshore wind forms. Wind Energy 9, 39–53. https://doi.org/10.1002/we.189.

Howland, Michael F., Lele, Sanjiva K., Dabiri, John O., 2019. Wind farm power optimization through wake steering. Proc. Natl. Acad. Sci. USA 116 (29), 201903680. https://doi.org/10.1073/pnas.1903680116.

Jacobsen, N.G., Fuhrman, D.R., Fredsøe, J., 2011. A wave generation toolbox for the opensource CFD library: OpenFoam. Int. J. Numer. Methods Fluid. 70, 1073–1088. https://doi.org/10.1002/fld.2726.

Jensen, N.O., 1983. A note on wind turbine interaction. In: Technical Report. Risø-M-2411. Risoe National Laboratory, Roskilde, Denm.

Jonkman, J. and Shaler, K.: FAST.Farm User's Guide and Theory Manual, Tech. Rep. NREL/TP-5000-7848, National Renewable Energy Laboratory, https://www.nrel.gov/docs/fy21osti/78485.pdf.

Krogstad, P.G., Eriksen, P.E., 2013. Blind test calculations of the performance and wake development for a model wind turbine. Renew. Energy 50, 325–333. https://doi.org/10.1016/j.renene.2012.06.044.

Larsen, G.C., 1988. A simple wake calculation procedure. In: Tech Note Risø-M-2760. Risø National Laboratory, Denmark.

Mehta, D., Zuijlen, A.V., Koren, B., Holierhoek, J.G., Bijl, H., 2014. Large eddy simulation of wind farm aerodynamics: a review. J. Wind Eng. Ind. Aerod. 133, 1–17. https://doi.org/10.1016/j.jweia.2014.07.002.

Menter, F.R., Kuntz, M., Langtry, R., 2003. Ten years of industrial experience with the SST turbulence model. In: Proceedings of the 4th International Symposium on Turbulence, Heat and Mass Transfer. Begell House Inc., West Redding, pp. 625–632.

Meyers, Meneveau, 2012. Optimal turbine spacing in fully developed wind farm boundary layers. Wind Energy 15, 305–317. https://doi.org/10.1002/we.469.

Neiva, A., Guedes, V., Massa, C.S., Freitas, D., 2019. A review of wind turbine wake models for microscale wind park simulation. In: 25th ABCM International Congress of Mechanical Engineering - COBEM.

Ott, S., 2011. Linearised CFD models for wakes. In: Tech Rep. Risø-R-1772(EN). Risø National Laboratory oai: pure.atira.dk:publications/c29803f3-a1eb-45ab-b73f-ede444928477.

Pierella, F., Krogstad, P.A., Saetran, L., 2014. Blind Test 2 calculations for two in-line model wind turbines where the downstream turbine operates at various rotational speeds. Renew. Energy 70 (oct), 62–77. https://doi.org/10.1016/j.renene.2014.03.034.

Porté-Agel, Bastankhah, M., Shamsoddin, S., 2020. Wind-Turbine and Wind-Farm Flows: A Review. Springer Netherlands. https://doi.org/10.1007/S10546-019-00473-0.

Sanderse, B., Pijl, S., Koren, B., 2011. Review of computational fluid dynamics for wind turbine wake aerodynamics. Wind Energy 14 (7), 799–819. https://doi.org/10.1002/we.458.

Sørensen, J.N., Shen, W.Z., 2002. Numerical modeling of wind turbine wakes, Journal of Fluids engineering. J. Fluid Eng. 124 (2) https://doi.org/10.1115/1.1471361.

Vatistas, G.H., 2006. Simple model for turbulent tip vortices. J. Aircraft 43 (5), 1577–1579. https://doi.org/10.2514/1.22477.

Wußow, S., Sitzki, L., Hahm, T., 2007. 3D-simulation of the turbulent wake behind a wind turbine. J. Phys. Conf. 75, 012033 https://doi.org/10.1088/1742-6596/75/1/012033.

Xie, S., Archer, C., 2015. Self-similarity and turbulence characteristics of wind turbine wakes via large-eddy simulation. Wind Energy 18 (10), 1815–1838. https://doi.org/10.1002/we.1792.